Highlights

Effect of turbulent Mach number on the thermodynamic fluctuations in canonical shock-turbulence interaction

Yogesh Prasaad M. S., Krishnendu Sinha

- Shock captured DNS at varying turbulent Mach number (M_t) and shock strengths (M)
- Scaled thermodynamic variances are found to increase with M_t in contrast to velocity
- Linear analysis (LIA) is used to investigate trend in thermodynamic variances
- Acoustic fluctuations added to LIA reproduces temperature and entropy variances
- LIA with all three Kovásznay modes matches the DNS pressure variance at high M_t

Effect of turbulent Mach number on the thermodynamic fluctuations in canonical shock-turbulence interaction

Yogesh Prasaad M. S., Krishnendu Sinha*

Department of Aerospace Engineering, Indian Institute of Technology Bombay, Mumbai 400 076, India.

Abstract

Shock waves can generate high levels of turbulent fluctuations in temperature, pressure and other thermodynamic properties. These have significant role in turbulent mixing, heat transfer and acoustic noise in high-speed flows. The thermodynamic fluctuations generated by canonical shock-turbulence interaction are strong functions of the shock strength and the upstream turbulence intensity. For a fixed shock Mach number, the downstream thermodynamic variances, normalized by the upstream turbulence kinetic energy, are found to increase with the incoming turbulent Mach number (M_t). This is in contrast to the trend observed for Reynolds stresses and the turbulent dissipation rate. We use direct numerical simulations and linear interaction analysis to investigate the effect of M_t on the post-shock thermodynamic field. It is found that the presence of small amount of acoustic and entropy fluctuations in the incoming flow can explain the high intensity of the post shock thermodynamic variances in the high M_t cases.

Keywords: compressible turbulence, shock waves, pressure fluctuations, temperature variance, Kovásznay modes, linear analysis

1. Introduction

Shock waves are ubiquitous in high-speed compressible flows; through which flow properties such as pressure and temperature undergo drastic

*Corresponding author

Email address: krish@aero.iitb.ac.in (Krishnendu Sinha)

changes. In case of a turbulent flow, the fluctuations in the flow properties are amplified across the shock, especially in the presence of a normal shock. A supersonic or hypersonic vehicle in cruise, interstellar accretion disks and volcanic eruptions are some examples, where one can find shock waves in a turbulent flow. An extensive discussion on Richtmyer-Meshkov instability (RMI) and its potential implications for the inertial confinement fusion (ICF) and astrophysical applications involving shock waves are provided in the two-part review by Zhou [1, 2]. The usefulness of shock waves in scramjet combustion, however, cannot be understated, especially in the mixing enhancement by turbulence generation [3, 4] and the ignition promotion by the temperature rise due to the passage of the shock wave [5]. Additional details on this subject can be found in the review article by Urzay [6]. Though a large wave drag is seen in supersonic/hypersonic vehicles due to shock waves, their formation is unavoidable in such vehicles. In practical scenarios, the interaction of turbulence and shock waves include non-uniform mean flow, streamline curvature, real gas effects, etc. The most fundamental problem is the case of isotropic turbulence interacting with a normal shock in a uniform mean flow, which is devoid of the above-mentioned complexities. Our model problem is this canonical shock-turbulence interaction, which provides a clean environment to study the effect of the shock wave on the turbulence and vice-versa.

In earlier studies [7, 8, 9, 10], computations for this canonical problem were carried out at very low turbulence intensities ($M_t \leq 0.2$). Lee *et al.* were the first to quantify the amplification of turbulence using shock-resolved simulations [7] and shock-captured simulations [8]. Mahesh *et al.* [9] showed that the negatively correlated entropy and vorticity fluctuations result in an enhanced turbulence amplification. The focus of these studies were also limited to the amplification of various statistical quantities related to velocity fluctuations such as shock-normal Reynolds stresses (R_{11}), vorticity variances ($\overline{\omega'^2}$) and turbulence kinetic energy (TKE). Recent studies have started to investigate the thermodynamic fluctuations in canonical shock-turbulence interaction. Quadros *et al.* [11, 12] studied the post-shock temperature (or energy) flux correlation using linear interaction analysis (LIA) and direct numerical simulation (DNS) data. They showed that the turbulent energy flux correlation is governed by the pressure - energy and pressure - dilatation source terms, which are dominated by the acoustic mode and can be reproduced well by LIA [11]. Tian *et al.* [13] investigated the turbulent mass flux (fluctuating density-velocity correlation) for a binary-fluid interacting with a normal shock and showed that the preferential distribution of TKE towards low-density regions and increased scalar dissipation rate results in mixing enhancement. Boukharfane *et al.* [14] independently studied the scalar dissipation rate for a similar problem and found that the preferential alignment of the vorticity vector due to the compression of the shock wave results in an enhanced mixing rate.

Using large-eddy simulations (LES), Braun *et al.* [15] compared computations with LIA and developed Reynolds-stress models to be used in the Reynolds-Averaged Navier-Stokes simulation (RANS) framework. Recently, Chen and Donzis [16] performed shock-resolved DNS at low Mach numbers for M_t as large as 0.54 and Re_λ up to 65. They compared various statistics including pressure and temperature with the Quasi-Equilibrium (QE) theory for shock-turbulence interaction developed by Donzis [17, 18]. They obtained functional forms for the instantaneous thermodynamic field in terms of M and M_t using the QE theory and truncated integrals for statistical moments.

Ryu and Livescu [19, 20] showed that the shock-normal Reynolds stress and transverse vorticity variances approach the LIA limit from below as the turbulent Mach number is reduced. This indicates that the non-linear terms result in reduced amplification of the quantities across the shock. A similar trend was also observed and reported by Larsson *et al.* [21] for the amplification of turbulent kinetic energy across the shock. The reason for this behavior was reported to be due to the reduction in mean jumps across the shock for intense upstream turbulence [22, 21]. Quadros *et al.* [11, 12] also observed similar trends for the shock-normal turbulent energy flux $(\overline{u'e'})$, where the correlation $\overline{u'e'}$ had reduced values for more intense turbulence levels upstream of the shock. This begs the question: whether all the fluctuations show reduced values for increasing M_t values upstream of the shocks ? We show in the following sections that this is not true for the thermodynamic fluctuations, which are dominated by acoustic and entropy effects.

The focus of the present work is to investigate the effect of turbulence intensity on the thermodynamic fluctuations (density, pressure, temperature, and entropy) behind the shock. We systematically vary the upstream turbulent Mach number M_t, and study the changes in the downstream thermodynamic variance relative to the incoming turbulent kinetic energy. Here, $M_t = \sqrt{R_{ii}}/\overline{a}$, with R_{ii} as the trace of the Reynolds stress tensor and $\widetilde{a}$ is the mean speed of sound. This is in continuation of our earlier work, where we studied the effect of shock strength on the fluctuating thermodynamic field by varying the mean flow Mach number, M [23]. We perform direct numerical simulations of canonical shock-turbulence interaction for a range of turbulent Mach numbers up to 0.40 at different shock Mach numbers. We use the term "DNS" in the extended sense, since the present simulations resolve the turbulence, but capture the shock waves. We continue to use the term "DNS" for simplicity, but it is to be taken as "shock-captured turbulence-resolved numerical simulations". In our earlier work [23], we used linear interaction analysis (LIA) with purely vortical turbulence upstream of the shock to understand the post-shock thermodynamic field in low M_t DNS data. For high M_t cases, LIA with only purely vortical upstream turbulence is found to be insufficient to determine the correct post-shock thermodynamic field. We show in this work that the other fundamental modes of Kovásznay [24], namely the acoustic and the entropy modes, are required in LIA to predict the post-shock thermodynamic fluctuations for high M_t cases.

A secondary objective of the present study is to show the effect of the acoustic and the entropy modes in the upstream turbulence on the post-shock thermodynamic field. Of particular interest is the upstream entropy mode and its correlation with the vortical disturbances, which has been found to significantly alter the turbulence kinetic energy amplification through a shock wave [25, 9]. The paper is organized as follows: Sect. 2 describes the numerical methodology and the statistical properties of the inflow turbulence. In Sect. 3, the effect of M_t on the thermodynamic fluctuations is discussed in detail, along with LIA results for comparable inflow turbulence. The upstream turbulence field is mostly vortical, with additional acoustic and entropy components as per the DNS data. The conclusions are presented in Sect. 4.

2. Methodology

We follow the numerical procedure similar to our earlier work [23]. The governing equations are the three-dimensional, unsteady, compressible Navier-Stokes (NS) equations with the assumption of perfect gas. The equations are solved in the Cartesian coordinates for the conservative variables, ρ, $\rho\, u_i$, $\rho\, E_0$

as shown below,

$$\frac{\partial \rho}{\partial t} + \frac{\partial (\rho\, u_k)}{\partial x_k} = 0, \tag{1a}$$

$$\frac{\partial (\rho\, u_i)}{\partial t} + \frac{\partial (\rho\, u_i u_k)}{\partial x_k} + \frac{\partial p}{\partial x_i} = \frac{\partial \sigma_{ik}}{\partial x_k}, \tag{1b}$$

$$\frac{\partial (\rho\, E_0)}{\partial t} + \frac{\partial (\rho\, u_k\, E_0)}{\partial x_k} + \frac{\partial (p\, u_k)}{\partial x_k} = \frac{\partial (u_i\, \sigma_{ik})}{\partial x_k} - \frac{\partial q_k}{\partial x_k}, \tag{1c}$$

where, ρ is density, u_i is the velocity vector, p is the pressure, E_0 is the total energy, σ_{ik} is the viscous stress tensor and q_k is the heat conduction vector. The viscous stresses and the heat flux are modeled using Stokes hypothesis and Fourier's law of heat conduction, respectively. They are expressed as follows,

$$\sigma_{ik} = \mu \left(\frac{\partial u_i}{\partial x_k} + \frac{\partial u_k}{\partial x_i} - \frac{2}{3} \frac{\partial u_m}{\partial x_m}\, \delta_{ik} \right), \tag{2a}$$

$$q_k = -\frac{\mu\, c_p}{Pr} \frac{\partial T}{\partial x_k}. \tag{2b}$$

State equation for the perfect gas holds and thus pressure, $p = \rho\, R\, T$. The thermal conductivity, κ is related to molecular viscosity, μ through the assumption of constant Prandtl number $Pr = \mu\, c_p/\kappa$, with c_p being the gas specific heat at constant pressure. The molecular viscosity varies as a function of temperature, which according to a power law is given as, $\mu_{ref}(T/T_{ref})^{3/4}$. Here, μ_{ref} and T_{ref} are the reference viscosity and temperature of the gas, respectively. A value of 0.7 is used as the Pr value.

The compressible NS equations are solved for a perfect gas (with $\gamma = 1.4$) in a three-dimensional rectangular domain of size, $k_0\, L_x = 9\pi$, $k_0\, L_y = k_0\, L_z = 8\pi$, where $k_0 = 4$ is the wavenumber corresponding to the maximum energy in the upstream turbulent field. Initially, the normal shock wave is placed close to the inflow at $k_0 x = 1\pi$. A non-reflective boundary condition is imposed in the form of a numerical sponge ($k_0\, x > 9\pi$), thereby neglecting any plausible reflection from downstream supporting conditions. Figure 1 shows the schematic of the computational domain. Periodic boundary conditions are applied in the shock-parallel directions.

The present set of computations is solved using the massively parallel solution-adaptive finite difference "Hybrid" solver [26, 21, 27]. The inviscid fluxes near the shock are calculated using a fifth order accurate weighted essentially non-oscillatory (WENO) numerical scheme with Roe flux splitting.

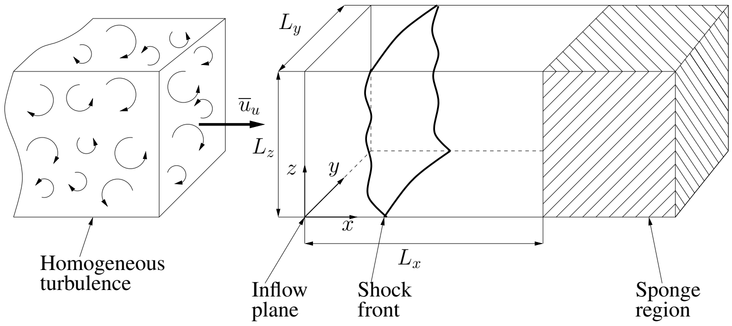

Figure 1: Schematic of the shock-turbulence interaction computational domain used in the numerical simulations

The fluxes in the remainder of the domain are calculated using a sixth order accurate central difference scheme in the split form proposed by Ducros *et al.* [28]. The shock wave(s) are identified as regions where the negative dilatation is greater than the low pass-filtered vorticity magnitude i.e., where $-(\partial u_k/\partial x_k) > \sqrt{\omega_k \omega_k}$ [21]. This shock-sensor is a modified form of the well-known Ducros sensor [29], which is able to distinguish weak compression waves from shock waves. The present shock-sensor is inspired by the observation that shock waves are associated with large negative dilatation (compression), whereas turbulence is more typically associated with large vorticity.

Having identified the grid points occupied by the shock wave(s), the WENO scheme is applied to the narrow region comprising those points as well as three additional grid points in every direction. This is carried out in order to ensure that the central scheme is never used across any shock wave(s). The switching between the WENO and central differencing schemes introduces internal 'interfaces' in the domain, where the method devised by Pirozzoli [30] is used to ensure proper conservation across these interfaces and their linear stability has been verified by Larsson and Gustafsson [31]. Any spurious oscillations that are introduced due to the solution-adaptive switching of the numerical schemes are thus bounded. It was also identified that the solution-adaptive method has no effect on the results provided that there is sufficient grid resolution [21]. The entire system of equations is integrated in time using a fourth order accurate explicit Runge-Kutta (RK4) scheme. This numerical procedure has been verified and validated on several problems of interest [32] and for the canonical shock-turbulence interaction

Table 1: List of cases simulated in the present study

M	M_t	$\frac{M_t}{(M-1)}$	Grid	$L_{\epsilon,u}/\eta_u$	η_d/η_u	$(k_{max}\eta_d)_{min}$
1.23	0.05	0.21	882×384^2	46	0.79	2.28
1.23	0.15	0.65	882×384^2	46	0.81	2.38
1.23	0.25	1.08	882×384^2	46	0.85	2.62
1.22	0.38	1.74	888×384^2	44	0.95	2.99
1.50	0.05	0.10	1042×384^2	46	0.65	1.86
1.50	0.15	0.30	1042×384^2	46	0.65	1.91
1.50	0.25	0.50	1042×384^2	44	0.70	2.11
1.50	0.39	0.80	1045×384^2	44	0.81	2.58
2.50	0.05	0.03	1142×384^2	46	0.47	1.33
2.50	0.16	0.10	1142×384^2	46	0.48	1.40
2.50	0.25	0.16	1142×384^2	44	0.49	1.48
2.50	0.39	0.26	1142×384^2	44	0.52	1.69
3.50	0.05	0.02	1313×384^2	46	0.44	1.26
3.50	0.16	0.06	1313×384^2	46	0.45	1.33
3.50	0.26	0.10	1313×384^2	45	0.46	1.39
3.50	0.39	0.16	1313×384^2	45	0.49	1.59

[26, 33, 21, 23].

We present DNS of canonical shock-turbulence interaction for upstream Mach number ranging from 1.23 to 3.5. The turbulent Mach number varies from $0.05-0.4$ for each case. The Reynolds number based on Taylor micro scale is in the range of $30-33$, and the Reynolds number based on dissipation length scale varies between 126 and 136. The list of cases simulated for the present study, along with the computational grid in each case, are provided in table 1. We use subscripts 'u' and 'd' to denote values immediately upstream and downstream of the shock, respectively. The dissipation length scale, $L_\epsilon = (0.5R_{kk})^{3/2}/\epsilon$ is shown as a ratio with the Kolmogorov scale, $\eta = \nu^{3/4}\epsilon^{-1/4}$ for the upstream region. Here, R_{kk} is twice the turbulent kinetic energy, ϵ is the turbulent dissipation rate and ν is the kinematic viscosity of the fluid. The reduction in Kolmogorov scale across the shock for each of the cases is shown and the quality of the grid to resolve the turbulent field determined by the maximum resolved wavenumber (k_{max}) [34, 13, 16] is shown the table.

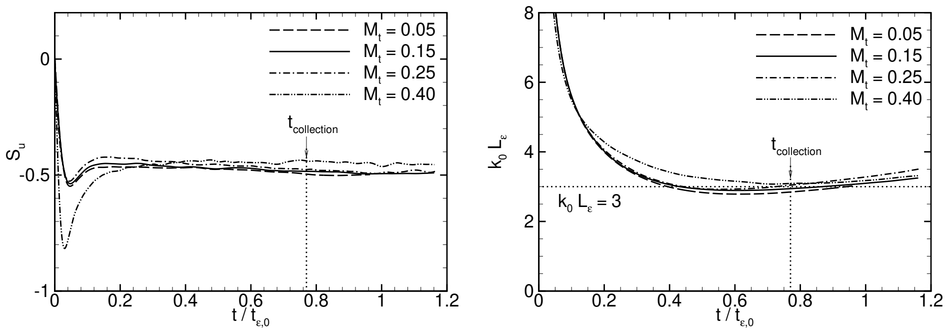

(a) Skewness of velocity derivatives

(b) Dissipation length scale

Figure 2: (a) Skewness of velocity derivatives (S_u) and (b) normalized dissipation length scale ($k_0 L_\epsilon$) against normalized time. Time is normalized by the initial dissipation timescale ($\tau_\epsilon = (R_{kk}/2)/\epsilon$ computed at $t = 0$)

2.1. Inflow turbulence

The inflow turbulence is generated separately on a triply periodic box of length, 2π with initial conditions provided using the method of Ristorcelli and Blaisdell [35]. We consider the von Kármán spectrum [33] given in Eq. (3) for generating the initial velocity field,

$$E(k) \sim \frac{1}{k_0} \frac{(k/k_0)^2}{\left[(k/k_0)^2 + 5/6\right]^{11/6}}, \tag{3}$$

where the maximum energy was specified at wavenumber, $k_0 = 4$. The turbulence was considered to be developed when the velocity derivative skewness, S_u settles around -0.5 (Fig. 2a), which is related to the small scales [36, 16]. Additionally, the development of large scales (which are much slower) was identified by the growth in the dissipation length scale, L_ϵ (Fig. 2b). The dotted line denoted by $t_{\text{collection}}$ in Fig. 2 marks the time at which the isotropic turbulence is collected to be used as inflow turbulence in the shock-turbulence interaction domain. At this instant of time, Re_λ is found to be approximately 34 for all cases.

The energy-spectrum function, $E(k)$ provides a much simpler but less complete description about the velocity fluctuations, whose integration over all wavenumbers provides the turbulent kinetic energy [37]. Figures 3a and 3b show the compensated energy spectrum for the total velocity fluctuations

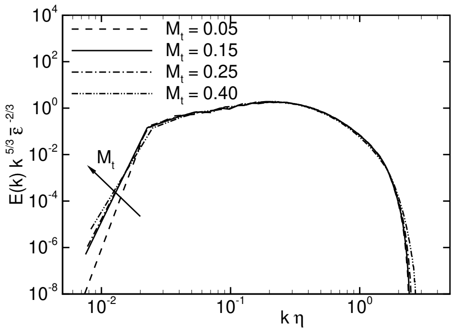

(a) Total energy

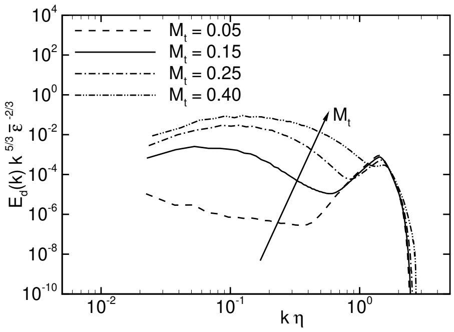

(b) Dilatational energy

Figure 3: (a) Compensated spectrum of the total kinetic energy ($E(k)$). (b) Compensated spectrum of the dilatational kinetic energy ($E_d(k)$). Grid is a triply periodic box of 384^3 size. The Kolmogorov constant for the highest M_t is 1.6 and 0.12 for the total and dilatation energies, respectively

($E(k)$) and that of the dilatational components ($E_d(k)$), respectively. The compensated energy spectrum is a normalized form of the energy spectrum function, usually shown to describe the distribution of the energy content in the fluctuations over the wavenumbers and is given by $E(k)k^{5/3}/\bar{\epsilon}^{2/3}$, where $\bar{\epsilon}$ is the mean dissipation rate. The compensated total energy spectra is similar to the low Reynolds number spectra observed in the forced isotropic turbulence simulations of Refs. [38, 39, 40]. The compensated spectra show increasing dilatational component in the velocity fluctuations (Fig. 3b) for increasing M_t in the turbulence fields. However, the dilatational energy is found to be an order of magnitude less than the solenoidal energy (compare the peak energy in Fig. 3b with that of Fig. 3a). It will be shown later that this increase in the dilatational energy results in increased dilatation variance and compressible part of the total energy.

Statistical convergence in shock-turbulence interaction simulations can be improved by using a longer database of isotropic turbulence. A single isotropic box, used in repetition to generate a longer database, is not statistically independent, i.e., the same statistics repeat after one time period of the turbulence box. A total of 8 statistically independent turbulence boxes are conjoined together at their ends using the method of Larsson [41] to obtain a homogeneous isotropic turbulence database. The blended turbulence is specified as the inflow turbulence using Taylor's hypothesis. Earlier com-

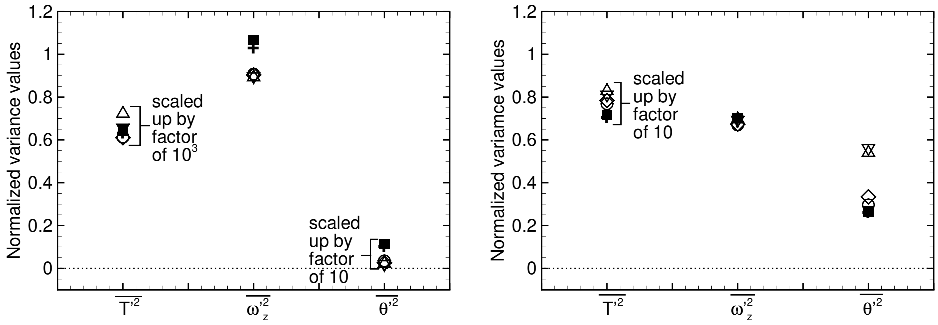

(a) $M_t = 0.05$

(b) $M_t = 0.40$

Figure 4: Variation of normalized temperature, vorticity and dilatation variances (a) $M_t = 0.05$ and (b) $M_t = 0.40$. Legend: isotropic turbulence (plusses), blended turbulence (filled squares), $M = 1.23$ (triangles), $M = 1.50$ (inverted triangles), $M = 2.50$ (diamonds) and $M = 3.50$ (circles)

putations of shock-turbulence interaction [26, 21, 14, 16] have also followed a similar procedure to provide long turbulence databases at the inflow.

Figure 4 shows the normalized temperature variance along with the transverse vorticity and dilatation variance for $M_t = 0.05$ and 0.40 cases. Data from the isotropic boxes (average of the 8 boxes), the blended database and the shock-turbulence interaction (just upstream of the mean shock) are shown in the figure. The temperature variance is normalized by $[(\gamma - 1)\,\overline{T}]^2$ as per linearized isentropic relations ($\rho'/\overline{\rho} = p'/(\gamma\,\overline{p}) = T'/[(\gamma-1)\,\overline{T}]$). The vorticity and the dilatation variances are normalized by $(k_0\overline{a})^2$, where $\overline{a}$ is the mean speed of sound. Here, the sound speed is chosen for consistent comparison between the turbulence databases and the shock-turbulence interaction data. The variances are additionally scaled by M_t^2 as followed in Refs. [26, 40, 21]. The other thermodynamic variances such as density and pressure show similar values as the temperature variance, when scaled according to the linearized isentropic relations. Temperature variance was scaled up by a factor of 10^3 (Fig. 4a) and 10 (Fig. 4b) for the $M_t = 0.05$ and 0.4 cases, respectively, whereas, the dilatation variance was scaled up by a factor of 10 in Fig. 4a to appear along with the vorticity variance in the same figure.

The temperature variance and the dilatation variance increase in magnitude for increasing M_t. The vorticity variance, on the other hand, is comparable between the two M_t cases for the turbulence databases. The

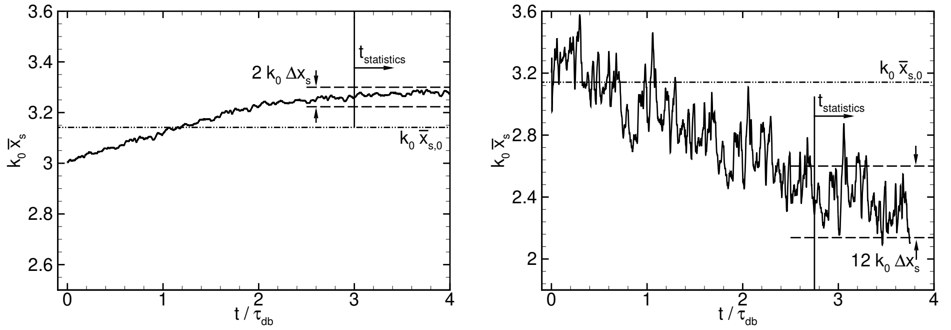

(a) $M_t = 0.05$ (b) $M_t = 0.40$

Figure 5: Variation of mean shock position against time from the dataset of $M = 1.23$ for (a) $M_t = 0.05$ and (b) $M_t = 0.40$. Here, $t_{\text{statistics}}$ represent the time from which statistics are computed

shock-turbulence interaction simulations show similar values as in the turbulence databases for the temperature and the vorticity variances (with only minor departures). The dilatation variance in the shock-turbulence interaction with $M_t = 0.05$ are negligible compared to the vorticity variance. For the $M_t = 0.40$ case, it is comparable to the vorticity variance for $M = 1.23$ and $M_t = 0.40$. As argued by Lee *et al.* [42], Taylor's hypothesis is not valid for the acoustic modes in compressible turbulence, which become more prominent at high $M_t/(M-1)$ cases (see table 1) and is reflected in the dilatation variances of the present DNS data.

2.2. Shock drift

A major numerical challenge in the high M_t simulations is the very large drift of the mean shock. The mean pressure at the outlet of the domain (backpressure) is not the same as the laminar pressure determined by the Rankine-Hugoniot condition specified at the initial time. Thus, the mean shock drifts away from its initial position depending on the backpressure value; sometimes the drift is so large that the mean shock can end up either at the inlet or at the sponge. A correct backpressure value is required to ensure that the shock is stationary, at least during the time-period at which the statistics are collected.

Chen and Donzis [16] used two numerical sponges to control the shock drift indirectly for their low M and high M_t simulations. We follow the trial and error approach of Larsson and Lele [26] with a single numerical sponge to sustain a stationary shock. The shock drift is controlled by an integral backpressure controller [26, 21] such that the mean drift speed of the shock is less than 0.15% of the mean shock-normal velocity upstream of the shock for the most intense turbulence case and much lower for weak turbulence intensities. This movement of the shock is illustrated in Fig. 5 for the dataset of $M = 1.23$, where the mean shock location is identified by the half mean pressure rise. The mean shock location ($\overline{x}_s$) is normalized by k_0 and the time is normalized by the inflow turbulence time period of $\tau_{db} = 8 \times 2\pi/\overline{u}_u$.

We observe that the shock drifts by a distance of one grid cell for the $M_t = 0.05$ case and up to eight grid cells for the $M_t = 0.40$ case during the time period of collection of statistics. At any instant of time, the cases with high local turbulence intensity ($M_t > 0.5(M-1)$) display very rapid displacement of the $y-z$ plane-averaged shock, ranging from 4 to 12 grid cells.

2.3. Grid convergence

Figure 6 shows the grid convergence for the normalized dissipation rate and the normalized temperature variance for the case $M = 1.23$ and $M_t = 0.40$, which is the case with the highest local turbulence intensity ($M_t/M = 0.31$). The statistics are obtained by averaging over the shock-parallel directions and time. Vorticity variance is normalized by $(k_0\overline{u}_u)^2$ and the temperature variance is normalized by $\overline{T}_d^2$. Additionally, they are also scaled by the upstream normalized TKE, $0.5\,\overline{u'^2_{i,u}}/\overline{u}_u^2$. The shock-normal direction is normalized by the peak energy wavenumber in the upstream turbulent field ($k_0 = 4$). The mean shock is identified using the mean dilatation profile, whose bounds are shown by the grey region in Fig. 6.

Grid convergence is carried out for the following grid sizes: 592×256^2, 888×384^2 and 1184×512^2, where the shock-normal grid-spacing at the shock ($\Delta x_s \approx \Delta y/1.75$) was determined using the approximate relation provided in Larsson and Lele [26]. Additionally, we also tested for the grid size of 1574×384^2, which has $\Delta x_s \approx \Delta y/3.5$, to prove that the grid size at the shock is sufficiently fine [43, 13]. The large-scale features such as Reynolds stresses and small-scale features such as the dissipation rate of TKE are also found to be grid-converged. The maximum difference in various statistics between grid sizes mentioned in the figure is found to be $\leq 4\%$. We find similar error values ($\sim 3-4\%$) for the $M = 1.50$ cases and much less for

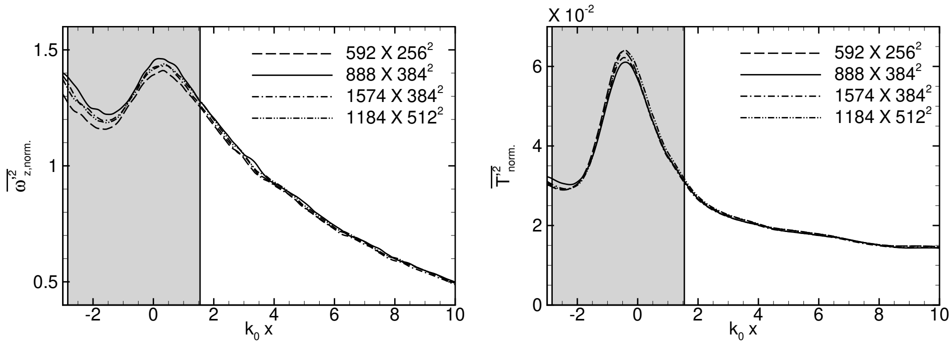

(a) Vorticity variance

(b) Temperature variance

Figure 6: Grid convergence test for the case of $M = 1.23$ and $M_t = 0.40$. (a) Normalized vorticity variance in the z-direction and (b) Normalized temperature variance. The grey region corresponds to the unsteady shock motion identified using the mean dilatation

the higher Mach numbers. Grid convergence test for the $M = 3.50$ and $M_t = 0.15$ case, which represents the low local turbulence intensity cases can be found in Ref. [23].

2.4. Linear analysis

The theoretical tool widely used to analyze shock-turbulence interaction is the linear interaction analysis. LIA was pioneered by Moore [44] and Ribner [45, 46] to study the interaction of planar waves with a shock wave. The tool has been extended to different types of problems [25, 47, 48, 49, 50, 51, 52, 53, 54]. Figure 7 shows the interaction of a single planar wave with a normal shock. The incident wave can be either vorticity, entropy, or acoustic and is characterized by its amplitude, $|A|$, the wavenumber vector, $\vec{k}$ and its orientation with respect to the shock-normal direction, ψ. Upon interaction, the shock deforms in response and all types of the Kovásznay modes are generated. The amplitudes of the post-shock waves are determined from the linearized Rankine-Hugoniot conditions. The post-shock characteristics of the acoustic, vorticity and entropy waves ($\vec{k}_a$, $\vec{k}_v$, $\vec{k}_s$ and ψ_a, ψ_v, ψ_s) are determined from the linearized Euler equations and the constraints at the shock wave. For the case of shock-turbulence interaction, the upstream turbulence is taken as a super-position of such planar waves, with each of them independently interacting with the shock. The post-shock statistics are computed by integrating over the energy spectrum. A detailed description

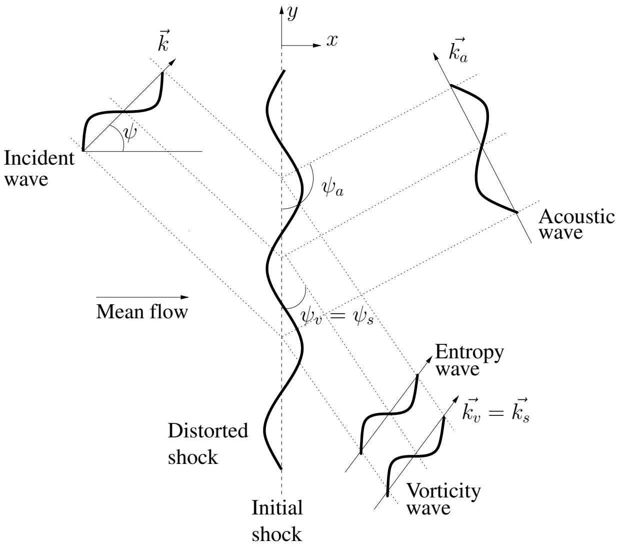

Figure 7: Schematic of a single planar wave interacting with a normal shock

of the procedure can be found in Mahesh *et al.* [25] and in Quadros *et al.* [11].

LIA is used to understand the fundamentals of shock-turbulence interaction [11, 12, 23, 55, 56], to model the unknown post-shock quantities [57, 58, 59, 60], to verify numerical simulations [13, 14], and as a surrogate for direct numerical simulations in the region of shock waves [19, 20, 15]. The analysis is based on linear and inviscid assumptions, such that the fluctuations are assumed to be small compared to the changes in the mean flow quantities across the shock. This limits the validity of LIA to low values of turbulent Mach numbers. The question about what is the threshold M_t value below which LIA can be taken to be accurate is still open. In this paper, we show that DNS cases with M_t as high as 0.4 can still be predicted by LIA, if the thermodynamic fluctuations in the upstream disturbance field are accounted for in the analysis.

3. Results and discussions

In this section, we present numerical simulation of the 16 cases of shock-turbulence interaction listed in table 1. We consider the thermodynamic quantities of density, pressure, temperature and entropy, and describe the effect of turbulent Mach number on their variances. Other relevant quantities like mass flux, heat flux and pressure-velocity correlation, can be derived from these four fundamental quantities, via suitable correlation coefficient. We attempt to reproduce the DNS data, especially the high M_t cases using LIA, by including all of the Kovásznay modes in the upstream turbulence.

3.1. Post-shock thermodynamic fluctuations

The spatial variation of thermodynamic variances from the DNS for the case of $M = 3.50$ and varying turbulent Mach numbers (M_t) is shown in Fig. 8. The density ($\overline{\rho'^2}$), pressure ($\overline{p'^2}$) and temperature ($\overline{T'^2}$) variances are normalized by the square of their downstream mean value ($\overline{\rho}_d^2$, $\overline{p}_d^2$, $\overline{T}_d^2$) and the normalized value of incident turbulence TKE. The entropy variance ($\overline{s'^2}$) is normalized by c_p^2 and the normalized value of upstream TKE. Essentially, the variances are normalized as,

$$\frac{\overline{\rho'^2}/\overline{\rho}_d^2}{TKE_u/\overline{u}_u^2}, \quad \frac{\overline{p'^2}/\overline{p}_d^2}{TKE_u/\overline{u}_u^2}, \quad \frac{\overline{T'^2}/\overline{T}_d^2}{TKE_u/\overline{u}_u^2}, \quad \frac{\overline{s'^2}/c_p^2}{TKE_u/\overline{u}_u^2}, \tag{4}$$

where TKE_u is the upstream turbulent kinetic energy.

The post-shock thermodynamic variances are found to increase with increasing M_t. The effect is found to be most prominent for the pressure variance, which has a rapid decay immediately behind the shock (near-field) and attains asymptotic values in the far-field ($x \to \infty$). A similar variation is observed for the temperature and entropy variances immediately behind the shock, which also show a monotonically increasing behavior with M_t. A strong viscous dissipation in the high M_t cases, however, brings down $\overline{T'^2}$ and $\overline{s'^2}$ in the far-field region. The case of $M_t = 0.05$ shows a much slower decay compared to the other M_t cases, which can be understood from the relation that the dissipation rate of the turbulent kinetic energy, $\epsilon \propto M_t^3$ [61].

The density variance shows a qualitative change in its spatial profile for increasing M_t. A local post-shock peak is observed for low M_t cases, while a monotonically decaying profile is seen for the high M_t cases. From an earlier analysis [23], it has been observed that the interplay between the acoustic and entropy modes yield a post-shock peak in the density variance, similar to the Reynolds stress profiles. The probable cause for the disappearance of the post-shock peak at high M_t is that the contribution of the acoustic modes has become larger than that of the entropy modes. This point is explored further in subsequent sections.

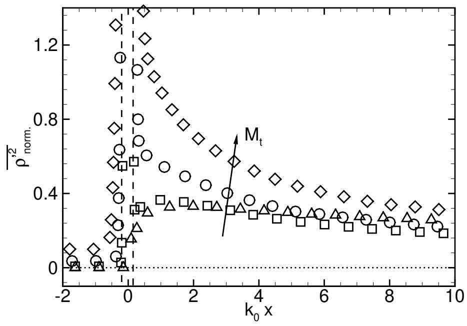

(a) Density variance

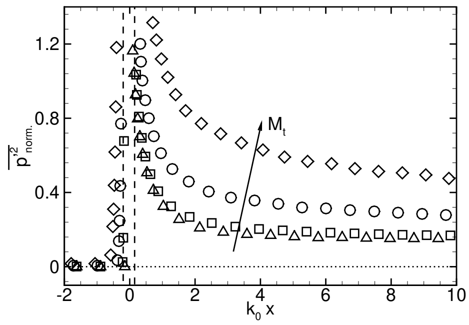

(b) Pressure variance

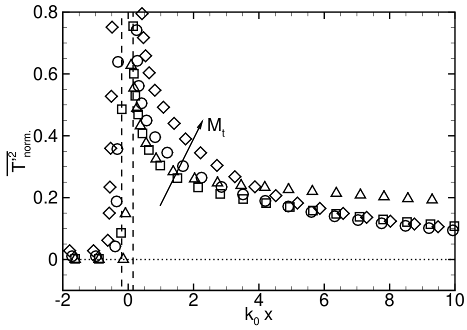

(c) Temperature variance

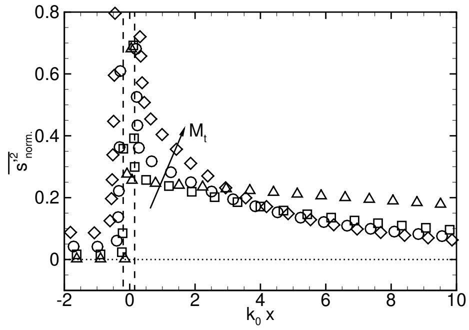

(d) Entropy variance

Figure 8: Spatial variation of the normalized thermodynamic variances for $M = 3.50$ and varying turbulent Mach numbers. Legend: $M_t = 0.05$ - triangles, $M_t = 0.15$ - squares, $M_t = 0.25$ - circles, and $M_t = 0.40$ - diamonds. The vertical dashed lines around $k_0x = 0$ denote the unsteady region of the shock in the $M_t = 0.05$ case

The qualitative variation of the thermodynamic variances with M_t is in direct contrast with that of the turbulence quantities related to velocity fluctuations. Ryu and Livescu [19] showed that amplification of the Reynolds stresses ($\overline{\rho}\, R_{ij} = \overline{\rho\, u_i'\, u_j'}$) and vorticity variances ($\overline{\omega'^2}$) decrease with increasing M_t values. The thermodynamic variances, on the other hand, display increased values for increasing M_t values. This is true when both velocity/vorticity and thermodynamic variances are normalized in the same way, which is by the square of their local mean values and scaled by the upstream TKE.

3.2. Upstream thermodynamic field

The upstream thermodynamic variances also show a monotonic increase with M_t (see Fig. 8 for $k_0 x < 0$ and columns $4-7$ in table 2) for a particular mean flow Mach number. We analyze the incoming turbulent field as a combination of vorticity, entropy, and acoustic components. The decomposition of the turbulent field into the three fundamental modes is based on Kovásznay's analysis [24]. It is used in the linear interaction analysis (LIA) framework to study shock-turbulence interaction [11, 12]. By quantifying the amount of vorticity, entropy and acoustic contributions in the upstream turbulent field, we attempt to address the qualitative and quantitative changes observed in the downstream thermodynamic field for increasing M_t.

Mahesh *et al.* [25] extended LIA to include the effect of entropy waves in the upstream solenoidal turbulence. In the present study, we follow the same approach to include the effects of the entropy mode over a purely vortical LIA (representative of low M_t cases), i.e., entropy fluctuations added to the hydrodynamic turbulence. Generally, the vorticity and entropy fluctuations in the upstream turbulence are written in terms of normal modes as

$$\frac{\omega_u'}{k\,\overline{u}_u} = A_v\, e^{\left(\mathrm{i}\,\vec{k}.\vec{r} - \mathrm{i}\,\Omega\, t\right)}, \tag{5}$$

$$\frac{s_u'}{c_p} = A_e\, e^{\left(\mathrm{i}\,\vec{k}.\vec{r} - \mathrm{i}\,\Omega\, t\right)}, \tag{6}$$

where A_v and A_e are the complex amplitudes of the vorticity and the entropy fluctuations, respectively, $\vec{r}$ is the direction vector, $\vec{k}$ is the wavenumber vector and Ω is the angular frequency of a wave in the upstream turbulence. The angular frequency obeys the dispersion relation, $\Omega = \vec{k}.\vec{u}$ for the vorticity and the entropy waves, and $\Omega = \vec{k}.\vec{u} \pm \overline{a}\, k$ for the acoustic waves [62].

Table 2: Normalized rms values of velocity and thermodynamic fluctuations upstream of the shock

M	M_t	$\dfrac{u'^{rms}_{1,u}}{\overline{u}_u}$	$\dfrac{\rho'^{rms}_u}{\overline{\rho}_u}$	$\dfrac{p'^{rms}_u}{\overline{p}_u}$	$\dfrac{T'^{rms}_u}{\overline{T}_u}$	$\dfrac{s'^{rms}_u}{c_p}$	$\lvert A_r\rvert$	ϕ_r	χ
1.23	0.05	0.0248	0.0012	0.0015	0.0006	0.0005	0.0409	1.5453	0.0004
1.23	0.15	0.0719	0.0125	0.0156	0.0054	0.0040	0.1403	1.5716	0.0052
1.23	0.25	0.1188	0.0450	0.0599	0.0191	0.0104	0.3087	1.6043	0.0284
1.22	0.38	0.1812	0.0999	0.1341	0.0422	0.0222	0.4593	1.6959	0.0644
1.50	0.05	0.0204	0.0012	0.0014	0.0005	0.0005	0.0473	1.5423	0.0003
1.50	0.15	0.0589	0.0119	0.0147	0.0052	0.0040	0.1633	1.5690	0.0046
1.50	0.25	0.0974	0.0438	0.0580	0.0186	0.0104	0.3655	1.5553	0.0266
1.50	0.39	0.1511	0.1081	0.1449	0.0451	0.0235	0.5805	1.5835	0.0687
2.50	0.05	0.0123	0.0011	0.0013	0.0005	0.0005	0.0750	1.5456	0.0003
2.50	0.16	0.0356	0.0114	0.0139	0.0050	0.0040	0.2591	1.5625	0.0040
2.50	0.25	0.0583	0.0418	0.0550	0.0178	0.0104	0.5807	1.5581	0.0238
2.50	0.39	0.0894	0.1030	0.1382	0.0435	0.0228	0.9404	1.6015	0.0650
3.50	0.05	0.0088	0.0011	0.0013	0.0005	0.0005	0.1044	1.5517	0.0003
3.50	0.16	0.0256	0.0114	0.0137	0.0050	0.0040	0.3582	1.5630	0.0039
3.50	0.26	0.0418	0.0413	0.0543	0.0177	0.0105	0.7981	1.5629	0.0229
3.50	0.39	0.0638	0.1020	0.1366	0.0432	0.0230	1.2991	1.5872	0.0630

Here, k denotes the magnitude of the wavenumber vector and $\overline{a}$ is the mean sound speed.

The relative magnitude of the vorticity and entropy waves in the upstream turbulence is given by

$$|A_r| = \frac{|A_e|}{|A_v|} = \sqrt{2}\,\frac{\sqrt{\overline{\rho_u'^2}}/\overline{\rho}_u}{\sqrt{\overline{u_{i,u}'^2}}/\overline{u}_u}. \tag{7}$$

The normalized density fluctuation for the $M = 1.23$ flow increases by an order of magnitude from the $M_t = 0.05$ case to the $M_t = 0.40$ case. For a fixed M_t, the normalized density fluctuations remain the same for different Mach numbers. The decrease in the normalized velocity fluctuations for increasing M values, however, results in an increasing $|A_r|$ value at high Mach numbers. Thus, $|A_r|$ is a function of both M and M_t. It attains a value of 0.46 for $M_t = 0.38$ at $M = 1.23$, indicating a substantial entropy component in the upstream turbulence. For the $M = 3.5$, $M_t = 0.39$ case, $|A_r|$ exceeds 1 and suggests a dominant effect of upstream entropy fluctuations.

In a uniform mean flow, vorticity and entropy waves travel at the same velocity as that of the mean flow. This implies that at any instant of time, the vorticity and the entropy waves are related to each other with a phase difference denoted by $\phi_r \in [0, \pi]$ with 0 and π being the in-phase and out-of-phase limits, respectively. The phase difference, ϕ_r can be determined from the DNS data (in the averaged sense) by

$$\phi_r = \frac{\overline{\rho_u' u_u'}}{\sqrt{\overline{\rho_u'^2}}\sqrt{\overline{u_u'^2}}}, \tag{8}$$

where $\overline{\rho_u' u_u'}$ is the turbulent mass-flux correlation in the shock-normal direction and the denominator comprises of the product of the rms values of upstream density and shock-normal velocity fluctuations. The value of ϕ_r is found to be close to $\pi/2$ radians (between 87° - 90°) for all the cases (see column 9 in table 2). The phase difference is nearly invariant for M and M_t variations in the DNS cases, thus making its effect insignificant compared to A_r. We consider the two extreme limits of ϕ_r in our combined vorticity and entropy analysis (shown in subsequent sections), such that the entire range of values that can be predicted are covered.

In a similar manner, the effect of acoustic modes can also be added to the purely vortical LIA procedure. The acoustic waves travel with their own sound speed in addition to the mean flow velocity, and thus are decorrelated from the vorticity and the entropy modes in the upstream turbulence. The extraction of the acoustic wave contribution to the upstream turbulent kinetic energy from the DNS data is not trivial. Instead, we follow the procedure of Quadros *et al.* [11] to obtain the upper bound of the mean acoustic contribution. The acoustic component of the TKE ($K_{A,u}$) is then computed as

$$K_{A,u} = \frac{1}{2}\left(\frac{1}{\gamma M}\right)^2 \frac{\overline{p_u'^2}}{\overline{p}_u^2}, \tag{9}$$

where the pressure field includes contributions from both the vortical motions (incompressible pressure) and the dilatational motions (compressible pressure). The value of $K_{A,u}$ obtained as such is therefore, the upper bound or the maximum value of the compressible TKE, under the assumption that the contribution of the kinematic fluctuations to the pressure field is small. The compressible TKE is then removed from the upstream total TKE ($K_{Tot,u}$) to obtain the TKE due to vorticity ($K_{V,u}$) or combined vorticity/entropy ($K_{V+E,u}$) cases. To this end, we define the compressible component of the total TKE as

$$\chi = \frac{K_{A,u}}{K_{Tot,u}}, \tag{10}$$

and the solenoidal component as

$$1 - \chi = \frac{K_{V,u}}{K_{Tot,u}}, \tag{11}$$

The largest possible contribution from the acoustic waves to the total TKE, even for the highest M_t case considered is $\mathcal{O}(10^{-2})$, and the upstream TKE is found to be mostly solenoidal in nature. It will be shown in the subsequent sections that this small contribution also yields large variations in the qualitative as well as the quantitative values of the post-shock thermodynamic variances. It is easily seen from table 2 (column 10) that χ is a function of M_t only, and increases by two orders of magnitude from 4×10^{-4} for $M_t = 0.05$ to 6.5×10^{-2} for the $M_t = 0.40$ case. The values remain approximately the same for all of the shock strengths considered, and thus remains invariant with M.

We hypothesize that LIA with a combination of different types of fluctuations in proper ratios would match the DNS cases with high M_t values. By this hypothesis, we imply that the purely vortical LIA would correspond to the very small M_t cases in the DNS. The purely acoustic LIA would then be described by very high M_t cases, but with an added constraint that only positive instantaneous pressure values are allowed. The effect of pure entropy waves on various quantities of interest is found to be small compared to the vorticity waves (see Mahesh *et al.* [25]), and thus the contribution of the entropy waves is always considered in conjunction with the vorticity waves. The combined cases with the three waves are expected to fall in the range between purely vortical and purely acoustic case, as per the hypothesis.

Our observation of increased values of upstream thermodynamic fluctuations for increasing M_t values also supports the idea of LIA with fluctuations combined in proper ratios. Consider the case of $M = 1.23$ in table 2, where the upstream normalized pressure fluctuations are at least an order of magnitude less than the shock-normal velocity fluctuations for the low M_t cases, and are of the same order for the high M_t cases. The increase in the rms values of upstream normalized pressure and entropy fluctuations with M_t results in increased values of χ and A_r, clearly indicating that the acoustic and the entropy modes are to be included in the LIA procedure.

3.3. Effect of upstream acoustic fluctuations

We consider the effect of acoustic fluctuations in the upstream turbulence first and compare it against the purely vortical LIA to explain the M_t trend observed in the DNS. Figure 9 shows the spatial comparison of purely acoustic fluctuations ($\mathrm{LIA_A}$) and purely vortical fluctuations ($\mathrm{LIA_V}$) in the upstream turbulence with the DNS dataset of $M = 2.50$ case. The $\mathrm{LIA_V}$ case is found to match well for the DNS data with low M_t values, which is clearly observed in the pressure variance (Fig. 9b) and the density variance (Fig. 9a) plots. The low M_t cases for the $M = 2.50$ case show a post-shock peak in the density variance profile, but the peak is not very distinct as seen in the case of $M = 3.50$ (Sect. 3.1). The temperature variance (Fig. 9c) and entropy variance (Fig. 9d) show a good match between $\mathrm{LIA_V}$ and $M_t = 0.05$ case in the region near the shock. Further downstream of the shock, both of these variances systematically deviate from the inviscid far-field value predicted by $\mathrm{LIA_V}$ due to the viscous decay in the DNS.

$\mathrm{LIA_A}$ predicts very high post-shock values for the thermodynamic variances and is at least a factor of 2 larger than those predicted by $\mathrm{LIA_V}$. The very high values predicted by $\mathrm{LIA_A}$ supports our earlier hypothesis that the upstream turbulence with only acoustic waves forms the upper bound for LIA predictions of thermodynamic variances. The turbulence with only vorticity

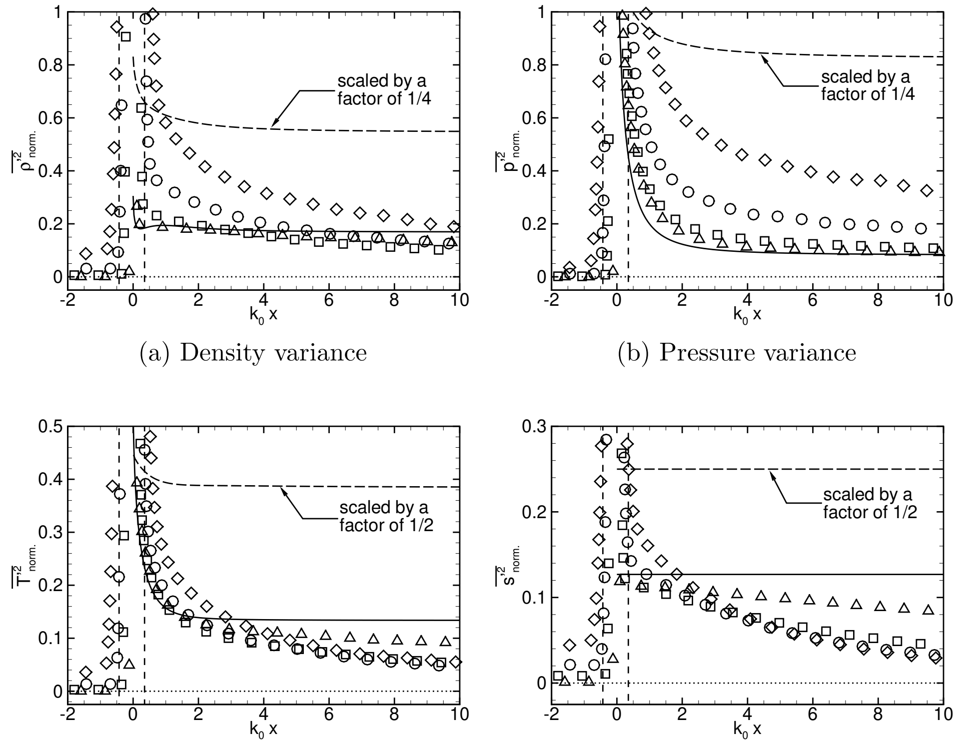

(a) Density variance

(b) Pressure variance

(c) Temperature variance

(d) Entropy variance

Figure 9: Spatial variation of the normalized thermodynamic variances for $M = 2.50$ and varying turbulent Mach numbers. The symbols remain the same as mentioned in Fig. 8 and the unsteady region of the shock is shown for the $M_t = 0.15$ case. Line legend: pure vorticity - solid line, pure acoustic - dashed line, DNS - symbols

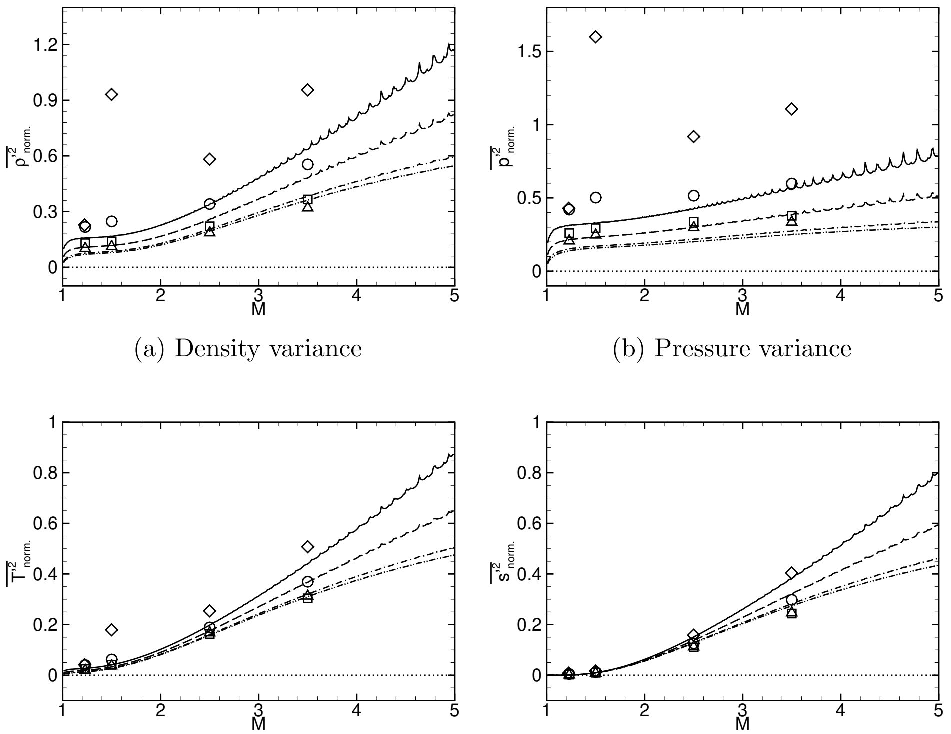

(a) Density variance

(b) Pressure variance

(c) Temperature variance

(d) Entropy variance

Figure 10: Effect of turbulent Mach number on the variation of the normalized thermodynamic variances with Mach number. Line legend: $\mathrm{LIA}_{\mathrm{V+A}}$ with $\chi = 0.0004$ - dash-double dotted line, 0.005 - dash-dotted line, 0.03 - dashed line, 0.06 - solid line and DNS - symbols. Symbols are the same as in Fig. 8

waves possibly forms the lower bound. The density variance predicted by $\mathrm{LIA}_{\mathrm{A}}$ (Fig. 9a dashed black line) has an exponential decay behind the shock, in contrast to the $\mathrm{LIA}_{\mathrm{V}}$ predictions (solid black line), which has a small post-shock peak after an initial decay. The exponentially decaying profile of the $\mathrm{LIA}_{\mathrm{A}}$ matches qualitatively with that of the high M_t DNS cases; suggesting that the acoustic contribution to the upstream turbulence need to be considered at high M_t.

We combine the $\mathrm{LIA}_{\mathrm{A}}$ and $\mathrm{LIA}_{\mathrm{V}}$ predictions for the thermodynamic variances according to

$$\frac{\overline{f'^2}}{\overline{f}^2} = (1-\chi)\left(\frac{\overline{f'^2}}{\overline{f}^2}\right)_V + \chi\left(\frac{\overline{f'^2}}{\overline{f}^2}\right)_A , \tag{12}$$

where the subscript V denotes the results obtained from LIA_V and the subscript A corresponds to LIA_A (see Refs. [25, 11] for details on this combination). The values of χ for each of the M_t cases are taken from the DNS data provided in the last column of table 2. We plot the variation of the combined vorticity and acoustic turbulence, $\text{LIA}_\text{V+A}$ against Mach number in Fig. 10 along with the DNS data for each of the M_t cases. The $\text{LIA}_\text{V+A}$ and the DNS data are taken at a representative location, $k_0 x = 1$.

Increased values of χ in $\text{LIA}_\text{V+A}$ show relatively higher values of the thermodynamic variances, which are closer to the high M_t DNS cases. Temperature (Fig. 10c) and entropy (Fig. 10d) variances predicted by $\text{LIA}_\text{V+A}$ match well with the DNS cases for the corresponding χ values. The density (Fig. 10a) and pressure (Fig. 10b), on the other hand, show a similar qualitative trend, but $\text{LIA}_\text{V+A}$ underpredicts the DNS data, especially for the high M_t cases (see diamond symbols and solid lines in Fig. 10). We next study the effect of upstream entropy fluctuations to explain the mismatch between LIA and DNS.

3.4. Effect of upstream entropy fluctuations

We first study the effect of the entropy mode at a representative value of $|A_r| = 0.45$ for $M = 3.5$ case. The combined case of vorticity and entropy, $\text{LIA}_\text{V+E}$ also depends on the phase-difference (ϕ_r). Figure 11 shows the comparison of $\text{LIA}_\text{V+E}$ for the three different phase-difference angles ($\phi_r = 0°, 90°$ and $180°$) with the LIA_V predictions.

In the majority of the cases, the addition of entropy fluctuations in the upstream turbulence increases the post-shock thermodynamic variances compared to the purely vortical case. The $\text{LIA}_\text{V+E}$ with $\phi_r = 0°$ exhibits a monotonic decay of $\overline{\rho'^2}$, as observed in the high M_t DNS data. The prediction is also close to the $\phi_r = 90°$ case, for $k_0 x > 2$. The $\phi_r = 0°$ temperature and entropy variances are also comparable to the $\phi_r = 90°$ case (the average phase difference computed from the DNS data, see table 2).

By comparison, the $\text{LIA}_\text{V+E}$ with $\phi_r = 180°$ gives very high post-shock variances for density, temperature and entropy. For pressure fluctuations, the predictions are lower than the vortical case, and almost negligible values for

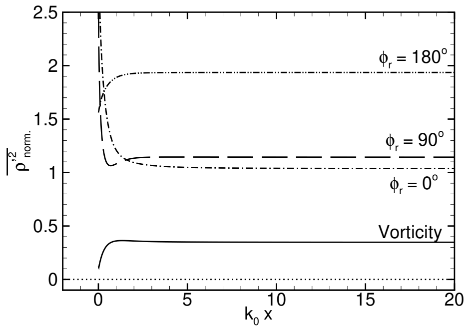

(a) Density variance

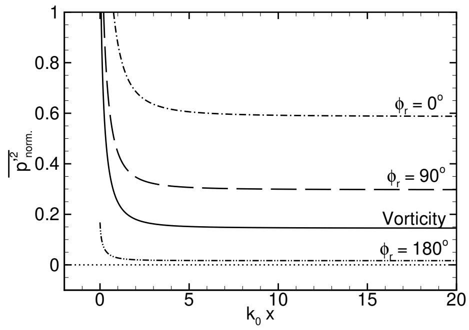

(b) Pressure variance

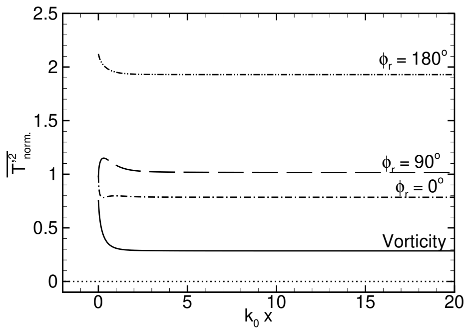

(c) Temperature variance

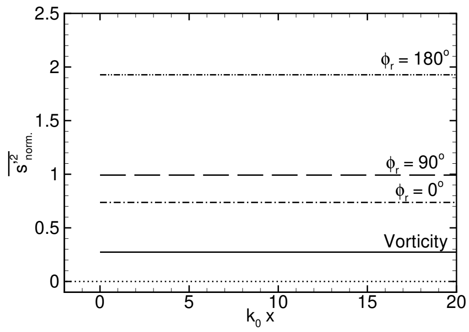

(d) Entropy variance

Figure 11: Spatial variation of the normalized thermodynamic variances from LIA of pure vorticity (solid) and vorticity/entropy turbulence interaction with a $M = 3.50$ normal shock. Combined vorticity/entropy turbulence have a constant amplitude of $|A_r| = 0.45$ (arbitrarily chosen) with phase difference of 0° (dash-dotted), 90° (long-dashed) and 180° (dash-double dotted) in the upstream region

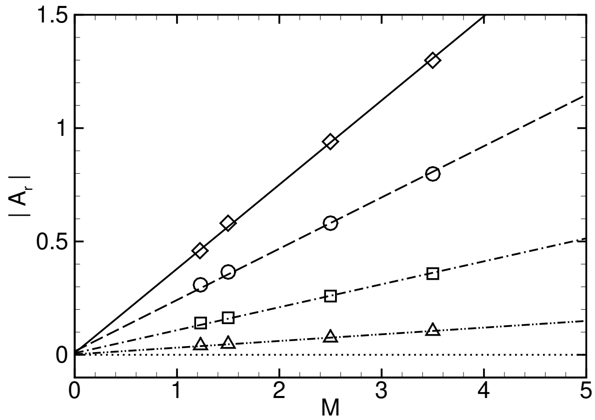

Figure 12: Variation of $|A_r|$ as a function of Mach number for each of the M_t cases. Symbols are the same as in Fig. 8. The lines correspond to linear curve fits for the $|A_r|$ values from the DNS: $M_t = 0.05$ - dash-double dotted, $M_t = 0.15$ - dash-dotted, $M_t = 0.25$ - dashed and $M_t = 0.40$ - solid

$k_0 x > 1$. In addition, the $\overline{\rho'^2}$ for $\phi_r = 180°$ does not match the exponential decay observed in the DNS data. The case of $\phi_r = 0°$ with varying $|A_r|$ is therefore considered for the analysis of the combined vorticity-entropy case. For a particular M_t value, $|A_r|$ varies as a linear function of Mach number in the DNS as shown in Fig. 12. The $\text{LIA}_{\text{V+E}}$ predictions with varying $|A_r|$ is compared against the DNS data for different M_t cases in Fig. 13.

Each of the thermodynamic variances show a significant increase in its value at higher $|A_r|$ values, which is representative of higher M_t values. The pressure variance (Fig. 13b) prediction by $\text{LIA}_{\text{V+E}}$ approaches the high values for the $M = 3.50$ DNS, but underpredicts at low Mach numbers and high M_t cases. The density variance (Fig. 13a), on the other hand, show relatively closer values for all Mach numbers up to $M_t = 0.25$ and overpredict the DNS data for $M_t = 0.40$. The case of $M = 1.50$ and $M_t = 0.40$ is an outlier, possibly due to the 'broken' shock nature (see Refs. [26, 21] for details on 'broken' shocks). The temperature (Fig. 13c) and the entropy (Fig. 13d) variance are similar to each other. $\text{LIA}_{\text{V+E}}$ grossly overpredicts DNS data for the higher M_t cases. The LIA predictions also appear to be qualitatively different than the Mach number trend observed in the DNS. The reason for these discrepancies is not known and is not pursued in this work. Instead, we focus on the density and pressure variances in the following section.

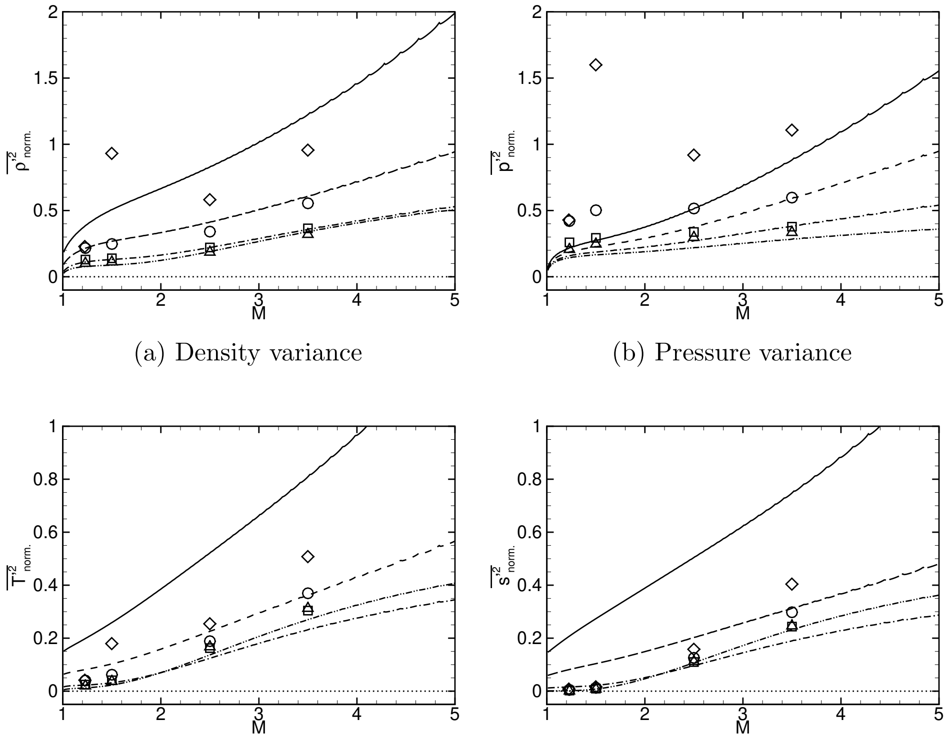

(a) Density variance

(b) Pressure variance

(c) Temperature variance

(d) Entropy variance

Figure 13: Effect of Mach number variation on the normalized thermodynamic variances at the location $k_0x = 1$ with $\phi_r = 0$. Symbols are the same as in Fig. 8. Lines correspond to the respective $|A_r|$ values for the M_t cases as shown in Fig. 12

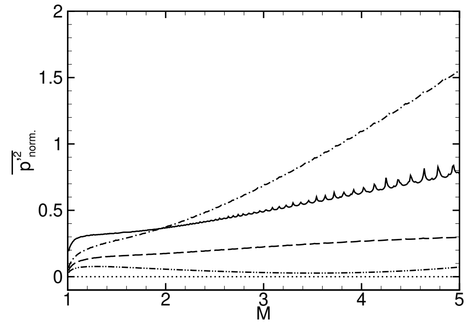

(a) Combination of two fluctuations

(b) Combination of all fluctuations

Figure 14: Effect of Mach number variation on the normalized pressure variance at the location $k_0x = 1$ for the case of $M_t = 0.4$. (a) $\mathrm{LIA_V}$ (dashed), $\mathrm{LIA_{V+A}}$ with $\chi = 0.063$ (solid), and $\mathrm{LIA_{V+E}}$ with varying $|A_r|$ for 0° (dash-dotted) and 180° (dash-double dotted) phase-differences. (b) $\mathrm{LIA_{V+E+A}}$ with base vorticity/entropy case of varying $|A_r|$ and $\phi_r = 0°$. The added acoustic contributions are $\chi = 0.0003$ (dashed), 0.0229 (dash-dotted), and 0.0630 (solid)

3.5. Effect of upstream acoustic and entropy fluctuations

We investigate the LIA predictions for the highest M_t case by including all three components in proper ratios as per the values given in table 2. Figure 14a summarizes the contribution of the different upstream modes for the pressure variance. The $\mathrm{LIA_V}$ prediction shown by a dashed line in the figure is bounded by $\mathrm{LIA_{V+E}}$ cases with $\phi_r = 0°$ (upper limit) and 180° (lower limit). This is similar to the spatially varying profile of $\overline{p'^2}$ shown in Fig. 11b. The $\mathrm{LIA_{V+A}}$ predicts a rapid increase in $\overline{p'^2}$ at very low Mach numbers and a relatively slower increase at high Mach numbers. The combined vorticity and acoustic case is also bounded between the two limits of the vorticity/entropy case, especially at high Mach numbers.

Figure 14b shows the combined effect of vorticity, entropy and acoustic modes in the upstream turbulence for the normalized pressure variance. The effect of each of the fundamental modes is combined according to

$$\left(\frac{\overline{p'^2}}{\overline{p}^2}\right)_{V+E+A} = (1-\chi)\left(\frac{\overline{p'^2}}{\overline{p}^2}\right)_{V+E} + \chi\left(\frac{\overline{p'^2}}{\overline{p}^2}\right)_{A}, \tag{13}$$

where

$$1-\chi = \frac{K_{V+E,u}}{K_{Tot,u}} = \frac{K_{V,u}}{K_{Tot,u}}, \tag{14}$$

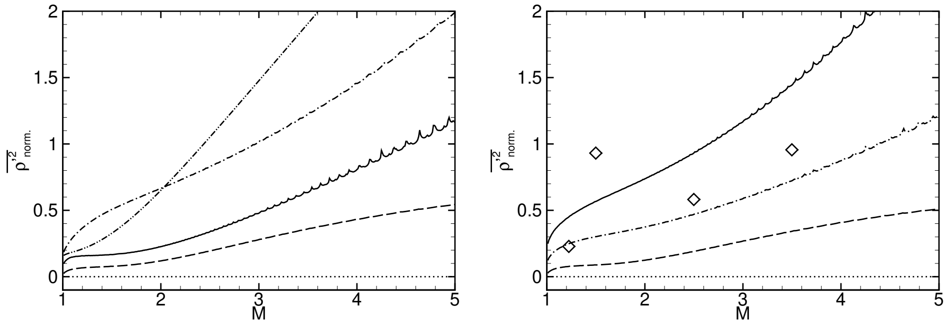

(a) Combination of two fluctuations

(b) Combination of all fluctuations

Figure 15: Effect of Mach number variation on the normalized density variance at the location $k_0x = 1$ for the case of $M_t = 0.4$. All other details are similar to Fig. 14

due to the fact that the pure entropy case has no TKE upstream of the shock (in the linear sense). The definition of χ remains the same as provided in Eq. (10) and represents the maximum possible acoustic contribution to the total TKE.

The different χ values used in Fig. 14b represent different levels of compressibility in the incoming turbulence field. The $\chi = 0.0003$ predictions (representative of the $M_t = 0.05$ case) are nearly identical to the vortical case in Fig. 14a. Higher χ leads to an increase in the post-shock $\overline{p'^2}$ magnitude, while the qualitative variation with Mach number remains unchanged. The LIA predictions, including vortical, entropy and acoustic field with $\chi = 0.063$ (for the highest M_t cases in table 2) compares well for the DNS data. It reproduces the $M_t = 0.4$ data for Mach 1.23, 2.5 and 3.5 cases. The Mach 1.5 case seems to be an outlier, as mentioned before.

Figure 15a shows the predictions of LIA with different modes in the upstream turbulence for the density variance. The LIA_V predicts the lowest value of $\overline{\rho'^2}$, in contrast to the pressure variance shown in Fig. 14a. The $\text{LIA}_\text{V+A}$ with $\chi = 0.063$ is larger than LIA_V, but less than the $\text{LIA}_\text{V+E}$ predictions. The combined vorticity/entropy LIA with $\phi_r = 0°$ and $180°$ cases show the largest values at $k_0x = 1$. The case with $\phi_r = 180°$ shows a completely different trend from the other three cases.

The $\text{LIA}_\text{V+E+A}$ predictions for the density variance are shown in Fig. 15b, where $\phi_r = 0°$ and χ takes different values as in Fig. 14b. As earlier, the $\text{LIA}_\text{V+E+A}$ for the lowest value of χ is close to the vortical case, while the

$\chi = 0.0229$ is comparable to the $M_t = 0.4$ DNS data. The highest χ value overpredicts $\overline{\rho'^2}$ from DNS, except for Mach 1.5 (outlier case). It can be interpreted as the upper bound of the possible LIA predictions with combination of all three modes. This is because the value of χ is estimated from the maximum acoustic contribution to the upstream TKE in the DNS.

4. Conclusion

In this work, we present direct numerical simulation of canonical shock-turbulence interaction at high values of turbulence Mach number in the upstream flow. A range of shock strengths ($M = 1.23 - 3.5$) is considered, and the effect of turbulent Mach number on the post-shock thermodynamic variance is investigated. The DNS data are compared with linear theory predictions to understand the post-shock evolution of the thermodynamic fluctuations. For a fixed Mach number, the normalized post-shock thermodynamic variances are found to increase with M_t. This is in contrast to the trend observed in the velocity fluctuations, and is due to the dominant effect of the upstream acoustic and entropy fluctuations. The predictions of purely vortical LIA correspond to the very small M_t cases in the DNS, and form the lower bound for the DNS cases with finite M_t. Inclusion of the acoustic fluctuations in the upstream solenoidal turbulence reproduces the downstream temperature and entropy variances at higher M_t values. By including all three fundamental Kovásznay modes in right proportions, LIA is able to predict the DNS pressure variance at high M_t, and provide an upper bound for the density fluctuations.

Acknowledgments

The authors thank Dr. Johan Larsson, University of Maryland, College Park, USA for the "Hybrid" code and for the numerous discussions on this work. YP thank the C-DAC NPSF PARAM YUVA-II supercomputing facility, Pune, India for providing the required computational resources. YP and KS also thank the LRZ: Leibniz Supercomputing Centre, Munich, Germany for providing computational resources as part of the 4^{th} SFB TRR40 Summer Program 2017 held at TUM, Germany. YP also acknowledges the support from SpaceTime-2 supercomputing facility at IIT Bombay, India for the computing time.

References

[1] Y. Zhou, Rayleigh - Taylor and Richtmyer - Meshkov instability induced flow, turbulence, and mixing. I, Phys. Rep. 720 - 722 (2017) 1 – 136. doi:10.1016/j.physrep.2017.07.005.

[2] Y. Zhou, Rayleigh - Taylor and Richtmyer - Meshkov instability induced flow, turbulence, and mixing. II, Phys. Rep. 723 - 725 (2017) 1 – 160. doi:10.1016/j.physrep.2017.07.008.

[3] P. J. Martínez Ferrer, R. Buttay, G. Lehnasch, A. Mura, A detailed verification procedure for compressible reactive multicomponent Navier-Stokes solvers, Comput. Fluids 89 (2014) 88 – 110. doi:10.1016/j.compfluid.2013.10.014.

[4] O. Mathieu, J. M. Pemelton, G. Bourque, E. L. Petersen, Shock-induced ignition of methane sensitized by NO_2 and N_2O, Combust. Flame 162 (8) (2015) 3053 – 3070. doi:10.1016/j.combustflame.2015.03.024.

[5] C. Huete, A. L. Sánchez, F. A. Williams, J. Urzay, Diffusion-flame ignition by shock-wave impingement on a supersonic mixing layer, J. of Fluid Mech. 784 (2015) 74 – 108. doi:10.1017/jfm.2015.585.

[6] J. Urzay, Supersonic combustion in air-breathing propulsion systems for hypersonic flight, Annu. Rev. Fluid Mech. 50 (1) (2018) 593–627. doi:10.1146/annurev-fluid-122316-045217.

[7] S. Lee, S. K. Lele, P. Moin, Direct numerical simulation of isotropic turbulence interacting with a weak shock wave, J. Fluid Mech. 251 (1993) 533 – 562. doi:10.1017/S0022112093003519.

[8] S. Lee, S. K. Lele, P. Moin, Interaction of isotropic turbulence with shock waves: effect of shock strength, J. Fluid Mech. 340 (1997) 225 – 247. doi:10.1017/S0022112097005107.

[9] K. Mahesh, S. K. Lele, P. Moin, The influence of entropy fluctuations on the interaction of turbulence with a shock wave, J. Fluid Mech. 334 (1997) 353 – 379. doi:10.1017/S0022112097004576.

[10] S. Jamme, J.-B. Cazalbou, F. Torres, P. Chassaing, Direct numerical simulation of the interaction between a shock wave and various types of

isotropic turbulence, Flow, Turbul. Combust. 68 (3) (2002) 227 – 268. doi:10.1023/A:1021197225166.

[11] R. Quadros, K. Sinha, J. Larsson, Turbulent energy flux generated by shock/homogeneous-turbulence interaction, J. Fluid Mech. 796 (2016) 113 – 157. doi:10.1017/jfm.2016.236.

[12] R. Quadros, K. Sinha, J. Larsson, Kovasznay Mode Decomposition of Velocity-Temperature Correlation in Canonical Shock-Turbulence Interaction, Flow, Turbul. and Combust. 97 (3) (2016) 787 – 810. doi:10.1007/s10494-016-9722-9.

[13] Y. Tian, F. A. Jaberi, Z. Li, D. Livescu, Numerical study of variable density turbulence interaction with a normal shock wave, J. Fluid Mech. 829 (2017) 551–588. doi:10.1017/jfm.2017.542.

[14] R. Boukharfane, Z. Bouali, A. Mura, Evolution of scalar and velocity dynamics in planar shock-turbulence interaction, Shock Waves 28 (6) (2018) 1117–1141. doi:10.1007/s00193-017-0798-5.

[15] N. O. Braun, D. I. Pullin, D. I. Meiron, Large eddy simulation investigation of the canonical shock-turbulence interaction, J. Fluid Mech. 858 (2019) 500–535. doi:10.1017/jfm.2018.766.

[16] C. H. Chen, D. A. Donzis, Shock-turbulence interactions at high turbulence intensities, J. Fluid Mech. 870 (2019) 813–847. doi:10.1017/jfm.2019.248.

[17] D. A. Donzis, Amplification factors in shock-turbulence interactions: effect of shock thickness, Phys. Fluids 24 (1) (2012) 011705. doi:10.1063/1.3676449.

[18] D. A. Donzis, Shock structure in shock-turbulence interactions, Phys. Fluids 24 (12) (2012) 126101. doi:10.1063/1.4772064.

[19] J. Ryu, D. Livescu, Turbulence structure behind the shock in canonical shock-vortical turbulence interaction, J. Fluid Mech. 756 (2014). doi:10.1017/jfm.2014.477.

[20] D. Livescu, J. Ryu, Vorticity dynamics after the shock-turbulence interaction, Shock Waves 26 (3) (2016) 241 – 251. doi:10.1007/s00193-015-0580-5.

[21] J. Larsson, I. Bermejo-Moreno, S. K. Lele, Reynolds-and Mach-number effects in canonical shock-turbulence interaction, J. Fluid Mech. 717 (2013) 293 – 321. doi:10.1017/jfm.2012.573.

[22] S. K. Lele, Shock-jump relations in a turbulent flow, Phys. Fluids A 4 (12) (1992) 2900 – 2905. doi:10.1063/1.858343.

[23] Y. P. M. Sethuraman, K. Sinha, J. Larsson, Thermodynamic fluctuations in canonical shock–turbulence interaction: effect of shock strength, Theor. Comput. Fluid Dyn. 32 (5) (2018) 629 – 654. doi:10.1007/s00162-018-0468-y.

[24] L. S. G. Kovásznay, Turbulence in Supersonic Flow, J. Aeronaut. Sci. 20 (10) (1953) 657 – 674, 682, reprinted in *AIAA J.*, **41(7)**, 219-237, 2003. doi:10.2514/8.2793.

[25] K. Mahesh, P. Moin, S. K. Lele, The interaction of a shock wave with a turbulent shear flow, Tech. Rep. TF-69, Thermosciences Division, Department of Mechanical Engineering, Stanford University, Stanford, California 94305 (1996).

[26] J. Larsson, S. K. Lele, Direct numerical simulation of canonical shock/turbulence interaction, Phys. Fluids 21 (12) (2009) 126101. doi:10.1063/1.3275856.

[27] I. Bermejo-Moreno, J. Bodart, J. Larsson, B. M. Barney, J. W. Nichols, S. Jones, Solving the compressible navier-stokes equations on up to 1.97 million cores and 4.1 trillion grid points, in: Proc. Int. Conf. High Perform. Comput. Networking, Storage Anal., no. 62 in SC '13, ACM, New York, NY, USA, 2013, pp. 1 – 10. doi:10.1145/2503210.2503265.

[28] F. Ducros, F. Laporte, T. Soulères, V. Guinot, P. Moinat, B. Caruelle, High-Order Fluxes for Conservative Skew-Symmetric-like Schemes in Structured Meshes: Application to Compressible Flows, J. Comput. Phys. 161 (1) (2000) 114 – 139. doi:10.1006/jcph.2000.6492.

[29] F. Ducros, V. Ferrand, F. Nicoud, C. Weber, D. Darracq, C. Gacherieu, T. Poinsot, Large-Eddy Simulation of the Shock/Turbulence Interaction, J. Comput. Phys. 152 (2) (1999) 517 – 549. doi:10.1006/jcph.1999.6238.

[30] S. Pirozzoli, Conservative Hybrid Compact - WENO Schemes for Shock - Turbulence Interaction, J. Comput. Phys. 178 (1) (2002) 81 – 117. doi:10.1006/jcph.2002.7021.

[31] J. Larsson, B. Gustafsson, Stability criteria for hybrid difference methods, J. Comput. Phys. 227 (5) (2008) 2886 – 2898. doi:10.1016/j.jcp.2007.11.025.

[32] E. Johnsen, J. Larsson, A. V. Bhagatwala, W. H. Cabot, P. Moin, B. J. Olson, P. S. Rawat, S. K. Shankar, B. Sjögreen, H. C. Yee, X. Zhong, S. K. Lele, Assessment of high-resolution methods for numerical simulations of compressible turbulence with shock waves, J. Comput. Phys. 229 (4) (2010) 1213 – 1237. doi:10.1016/j.jcp.2009.10.028.

[33] J. Larsson, Effect of Shock-Capturing Errors on Turbulence Statistics, AIAA J. 48 (7) (2010) 1554 – 1557. doi:10.2514/1.J050004.

[34] V. Eswaran, S. B. Pope, An examination of forcing in direct numerical simulations of turbulence, Comput. Fluids 16 (3) (1988) 257–278. doi:10.1016/0045-7930(88)90013-8.

[35] J. R. Ristorcelli, G. A. Blaisdell, Consistent initial conditions for the DNS of compressible turbulence, Phys. Fluids 9 (1) (1997) 4 – 6. doi:10.1063/1.869152.

[36] S. Tavoularis, J. C. Bennett, S. Corrsin, Velocity-derivative skewness in small Reynolds number, nearly isotropic turbulence, J. Fluid Mech. 88 (1) (1978) 63. doi:10.1017/S0022112078001986.

[37] S. B. Pope, Turbulent flows, Cambridge University Press. Cambridge, UK, 2000.

[38] T. Gotoh, D. Fukayama, Pressure spectrum in homogeneous turbulence, Phys. Rev. Lett. 86 (17) (2001) 3775–3778. doi:10.1103/PhysRevLett.86.3775.

[39] D. A. Donzis, K. R. Sreenivasan, The bottleneck effect and the kolmogorov constant in isotropic turbulence, J. Fluid Mech. 657 (2010) 171–188. doi:10.1017/S0022112010001400.

[40] D. A. Donzis, S. Jagannathan, Fluctuations of thermodynamic variables in stationary compressible turbulence, J. Fluid Mech. 733 (2013) 221 – 244. doi:10.1017/jfm.2013.445.

[41] J. Larsson, Blending technique for compressible inflow turbulence: Algorithm localization and accuracy assessment, J. Comput. Phys. 228 (4) (2009) 933 – 937. doi:10.1016/j.jcp.2008.10.027.

[42] S. Lee, S. K. Lele, P. Moin, Simulation of spatially evolving turbulence and the applicability of Taylor's hypothesis in compressible flow, Phys. Fluids A 4 (7) (1992) 1521 – 1530. doi:10.1063/1.858425.

[43] E. Garnier, P. Sagaut, M. Deville, Large eddy simulation of shock / homogeneous turbulence interaction, Comput. Fluids 31 (2) (2002) 245 – 268. doi:10.1016/S0045-7930(01)00022-6.

[44] F. K. Moore, Unsteady oblique interaction of a shock wave with a plane disturbance, Tech. Rep. NACA TR 1165, NACA, supersedes *NACA TN 2879*, 1953 (1954).

[45] H. S. Ribner, Convection of a pattern of vorticity through a shock wave, Tech. Rep. NACA TR 1164, NACA, supersedes *NACA TN 2864*, 1953 (1954).

[46] H. S. Ribner, Spectra of noise and amplified turbulence emanating from shock-turbulence interaction, AIAA J. 25 (3) (1987) 436 – 442. doi:10.2514/3.9642.

[47] D. Fabre, L. Jacquin, J. Sesterhenn, Linear interaction of a cylindrical entropy spot with a shock, Phys. Fluids 13 (8) (2001) 2403 – 2422. doi:10.1063/1.1383592.

[48] J. Griffond, Linear interaction analysis applied to a mixture of two perfect gases, Phys. Fluids 17 (8) (2005) 086101. doi:10.1063/1.1997982.

[49] J. G. Wouchuk, C. Huete Ruiz de Lira, A. L. Velikovich, Analytical linear theory for the interaction of a planar shock wave with an isotropic turbulent vorticity field, Phys. Rev. E 79 (6) (2009) 066315. doi:10.1103/PhysRevE.79.066315.

[50] C. Huete Ruiz de Lira, A. L. Velikovich, J. G. Wouchuk, Analytical linear theory for the interaction of a planar shock wave with a two- or three-dimensional random isotropic density field, Phys. Rev. E 83 (5) (2011) 056320. doi:10.1103/PhysRevE.83.056320.

[51] C. Huete, J. G. Wouchuk, A. L. Velikovich, Analytical linear theory for the interaction of a planar shock wave with a two- or three-dimensional random isotropic acoustic wave field, Phys. Rev. E 85 (2) (2012) 026312. doi:10.1103/PhysRevE.85.026312.

[52] C. Huete, T. Jin, D. Martnez-Ruiz, K. Luo, Interaction of a planar reacting shock wave with an isotropic turbulent vorticity field, Phys. Rev. E 96 (5) (2017) 053104. doi:10.1103/PhysRevE.96.053104.

[53] N. Alferez, E. Touber, One-dimensional refraction properties of compression shocks in non-ideal gases, J. Fluid Mech. 814 (2017) 185–221. doi:10.1017/jfm.2017.10.

[54] C. Huete, E. Abdikamalov, D. Radice, The impact of vorticity waves on the shock dynamics in core-collapse supernovae, Mon. Not. R. Astron. Soc. 475 (3) (2018) 3305–3323. doi:10.1093/mnras/stx3360.

[55] E. Touber, N. Alferez, Shock-induced energy conversion of entropy in non-ideal fluids, J. Fluid Mech. 864 (2019) 807 – 847. doi:10.1017/jfm.2019.25.

[56] G. Farag, P. Boivin, P. Sagaut, Interaction of two-dimensional spots with a heat releasing/absorbing shock wave: linear interaction approximation results, J. Fluid Mech. 871 (2019) 865 – 895. doi:10.1017/jfm.2019.324.

[57] O. Soulard, J. Griffond, D. Souffland, Pseudocompressible approximation and statistical turbulence modeling: Application to shock tube flows, Phys. Rev. E 85 (2) (2012) 026307. doi:10.1103/PhysRevE.85.026307.

[58] J. Griffond, O. Soulard, Evolution of axisymmetric weakly turbulent mixtures interacting with shock or rarefaction waves, Phys. Fluids 24 (11) (2012) 115108. doi:10.1063/1.4767729.

[59] R. Quadros, K. Sinha, Modelling of turbulent energy flux in canonical shock-turbulence interaction, Int. J. Heat Fluid Flow 61, Part B (2016) 626 – 635. doi:10.1016/j.ijheatfluidflow.2016.07.006.

[60] K. Sinha, M. S. Yogesh Prasaad, Analysis and modeling of thermodynamic fluctuations generated by shock-turbulence interaction, in: AIAA Fluid Dyn., no. AIAA 2019-2155 in AIAA 2019 SCITECH Forum, San Diego, CA, USA, 2019. doi:10.2514/6.2019-2155.

[61] H. Tennekes, J. L. Lumley, A First Course in Turbulence, The MIT Press, Cambridge, Massachussetts, USA, 1972.

[62] J. F. McKenzie, K. O. Westphal, Interaction of Linear Waves with Oblique Shock Waves, Phys. Fluids 11 (11) (1968) 2350 – 2362. doi:10.1063/1.1691825.